Strong particle-hole asymmetry in a 200 Kelvin superconductor

Soham S. Ghosh, Yundi Quan, and Warren E. Pickett[*]
Department of Physics, University of California, Davis, California 95616, USA

The superconducting state of metals has long provided a classic example of particle-hole symmetry at low energy. Fermionic self-energy results based on first-principles theory for the electron-phonon coupling in H_3S presented here illustrate strong particle-hole asymmetry in the dynamics arising from the underlying sharp structure in the fermionic density of states. Thus H_3S not only is the superconductor with the highest critical temperature T_c (through 2018), but its low-energy, low-temperature properties deviate strongly from textbook behavior. The minor momentum and band dependence of the fermionic self-energy allows evaluation of the momentum-resolved and zone-averaged spectral densities and interacting thermal distribution function, all of which clearly illustrate strong particle-hole asymmetry.

I. BACKGROUND

The discovery [1] and confirmation [2,3] of a record high superconducting transition temperature as high as $T_c = 203$ K in H_3S at 160-GPa pressure has reignited efforts toward the long dreamed of pinnacle of superconductivity at room temperature. The conventional phonon-exchange mechanism of electron pairing confirmed by isotope shift measurements [1] and by several theoretical studies [4–13] belies the occurrence and interconnection of several *unconventional* processes competing within H_3S. This new phase of superconducting matter above 200 K arises from three causes: the small mass of the proton compared to that of typical nuclei, strong scattering by large H displacements, and sharp structure in the electronic density of states $N(E)$ at the Fermi energy E_F arising from a pair of closely spaced (300 meV) van Hove singularities (vHs). Each vHs occurs at 24 symmetry related points in the Brillouin zone (BZ), thereby involving a significant fraction of the Fermi surface with low carrier velocities [14]. The small proton mass elicits phenomena that have received detailed theoretical attention: high-frequency phonons; quantum zero-point motion [12] of H and its effect on crystal stability [15]; strong anharmonicity, which impacts dynamic crystal stability [12,15]; the character and coupling strength of phonons [4,8,12,15]; and the unsettled question of nonadiabatic effects due to vanishing velocities near E_F at 48 points in the BZ [14].

The effects of the vHs are neglected in most theoretical work, although every aspect of standard electron phonon coupling (EPC) theory requires reformulation when $N(E)$ varies strongly on the scale of phonon energies [16,17]. Momentum-dependent Eliashberg equations can be applied on the imaginary frequency axis [12,17], but the vHs make numerical convergence challenging. Additionally, the normally irrelevant Debye-Waller self-energy (SE) bubble diagram becomes relevant [12]. Also, the concept of phonon scattering electrons from Fermi surface to Fermi surface must be generalized because regions of the zone with energy within Ω (maximum phonon energy) of the Fermi surface contribute nonuniformly to scattering processes. In the case when only the fermionic density of states (DOS) but not the wave function character is strongly varying, as in H_3S [6,14], the theory has been generalized and was applied to Nb_3Sn [17], whose DOS peak is even sharper than in H_3S.

There has not yet been any study of the interacting fermionic excitation spectrum in H_3S that provides direct evidence of EPC. The pioneering work of Engelsberg and Schrieffer [18] and Shimojima and Ichimura [19] revealed how coupling results in mixed elementary excitations—fermionic quasiparticles incorporating lattice motion and renormalized (bosonic) phonons—that are each a combination of bare electrons and phonons, with their mixing increasing with the EPC strength λ. In this paper we address the excitation spectrum, with a description of (1) *sharpening, not broadening,* of the already narrow spectral peak by interactions, (2) the "waterfall" structure in the momentum-resolved spectral density as coherence burns off, and (3) several unconventional impacts of strong particle-hole (p-h) asymmetry.

Section II describes the computational methods that have been applied to evaluate the fermionic self-energy and the resulting spectral density. In Sec. III the self-energy is displayed and discussed, along with the interacting band structure and associated spectral density (the interacting counterpart of the electronic density of states). The effect of gap opening is also provided. The interacting thermal distribution function is provided and discussed in Sec. IV, illustrating its particle-hole asymmetry. In Sec. V we provide predictions for the infrared optical conductivity, and Sec. VI provides a succinct summary.

II. METHODS

Density functional theory based and density functional perturbation theory based computations have been carried

*wepickett@vcdavic.edu

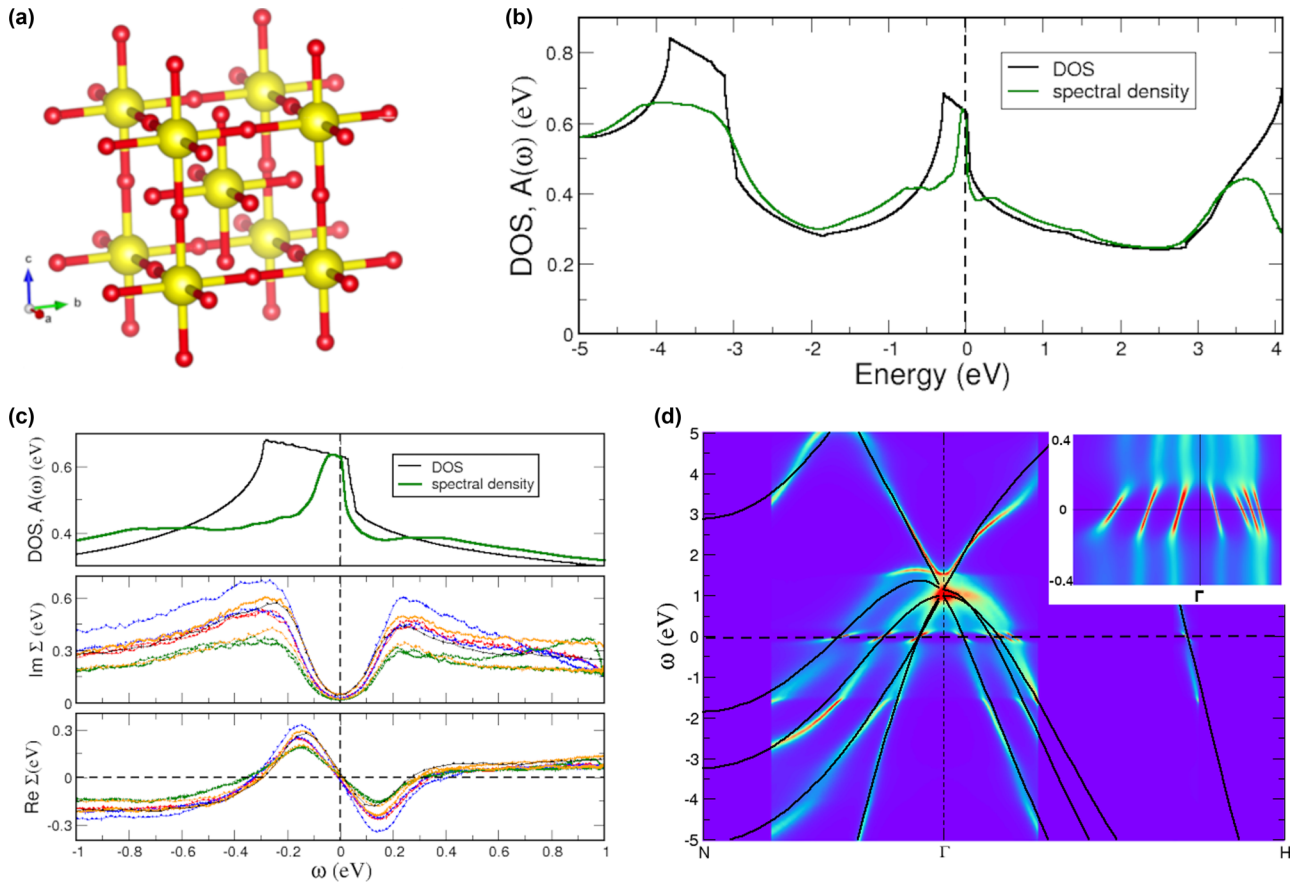FIG. 1. Electron self-energy $\Sigma_{\mathbf{k},\mathbf{n}}(\omega)$ and several consequences. (a) Crystal structure of $Im\bar{3}m$ H_3S with highlighted H-S bonds; large and small spheres represent S and H, respectively. The S atoms form a simple bcc lattice, and H atoms are located between two S atoms. (b) Spectral density $A(\omega)$ (see text) compared to the electronic DOS. Note the sharpness of the peak at E_F. (c) Bottom: $\mathrm{Re}\Sigma_{k,n}(\omega)$ for the five bands n crossing E_F plotted versus the frequency ω. Middle: $\mathrm{Im}\Sigma_{k,n}(\omega)$, obtained and plotted as for $\mathrm{Re}\Sigma_{k,n}(\omega)$. Top: the behavior of spectral density $A(\omega)$ and the electronic DOS near the E_F peak, showing the distinctive *narrowing* rather than broadening of the peak. (d) Band- (n) and momentum- ($\vec{k}$) resolved electron spectral function $A_{\vec{k},n}(\omega)$ calculated with EPW, overlaid on the uncoupled Kohn-Sham bands, along two high-symmetry lines. Colors at the red end of the rainbow spectrum are higher intensity. The renormalized slope at the Fermi level (see inset) is an indication of the factor of 3 $(1 + \lambda)$ mass enhancement caused by strong EPC. Farther than $\Omega \sim 250$ meV from the Fermi level, decay by phonon emission smears the single-particle states and removes the coherent renormalization.

out using a plane wave basis set in the QUANTUM ESPRESSO (QE) [20,21] simulation package, giving the electronic and phonon dispersions and EPC. H_3S at a pressure of 210 GPa has space group $Im\bar{3}m$ consisting of a bcc lattice with a lattice constant of 5.6 a.u. [6], pictured in Fig. 1(a). This structure and pressure have been used in the present calculations in harmonic approximation. Norm-conserving pseudopotentials of the Trouiller-Martins type are used in the QE code. The Perdew-Burke-Ernzerhof [22] implementation of the generalized gradient approximation is chosen as the exchange-correlation functional.

BCS theory, and its strong-coupling Migdal-Eliashberg extension [23,24], of phonon-coupled superconductivity provides a broad road map for achieving high critical temperature in conventional superconductors. Quantities related to EPC, such as the Eliashberg function $\alpha^2F(\omega)$, λ, the electron self-energy $\Sigma(\vec{k}, \omega)$, and resulting spectral functions in the normal state, were obtained using the QE, WANNIER90 [25], and EPW codes [24,26–28]. We have found that the vHs require unusually fine $\vec{k}$ (electron) meshes to obtain converged results.

Along with a plane wave basis set with a cutoff of 85 Ry we have used a $26 \times 26 \times 26$ **k**-point grid for the electronic self-consistent routines and a $32 \times 32 \times 32$ **k**-point grid for the DOS calculation. A $6 \times 6 \times 6$ **q**-point grid was used to calculate the phonon eigenvalues and dynamical matrices. The use of WANNIER90 and EPW allows us to interpolate the electron and phonon eigenvalues to a fine mesh of $60 \times 60 \times 60$ **k** and **q** points each for the final BZ integration. The band electronic spectrum $N(E)$ contains a narrow peak with Fermi energy (the zero of energy) lying at the higher of two vHs separated by 300 meV [14], shown on different scales in Figs. 1(b) and 1(c).

The EPW [26,27] code of Giustino and collaborators provides the electron momentum k and band index n self-energies on a dense BZ mesh. The weak k, n dependence of the electronic self-energy $\Sigma_{kn}(\omega)$ allows construction of a zone-averaged $\Sigma(\omega)$ that will provide the interacting electronic spectral function. The fermionic Green's function $G_{k,n}(\omega)$ provides the band electron spectral density $A_{k,n}(\omega)$ and thereby the zone-averaged counterpart $A(\omega)$.

III. ELECTRON SELF-ENERGY

Scatterplots of both the real and imaginary parts of $\Sigma_{kn}(\varepsilon_{kn})$ versus ε_{kn} are shown in Fig. 1(c) for the bands crossing μ (zero). The self-energies fall along lines for each band, with minor band dependence. This enables us to obtain a representative average $\Sigma(\omega)$.

The electron self-energy $\Sigma_{kn}(\omega) = M + i\Gamma$ gives the energy shift M and broadening Γ that provide insight into many consequences of EPC. The interacting Green's function is (suppressing all indices) $G^{-1} = G_{KS}^{-1} - \Sigma$ in terms of the Kohn-Sham (band) Green's function G_{KS}. In Fig. 1(c) these real and imaginary parts of $\Sigma_{kn}(\varepsilon_{kn})$, obtained using the EPW code in the normal state (200 K) of H_3S, are shown for each of the five bands crossing E_F. The EPW code produces matrix elements of Σ in the DFT band representation $\Sigma_{k,n}(\omega)$ for each band state $\vec{k}$, n at $\omega = \varepsilon_{kn}$.

The band dependence is roughly an average value $\Sigma(\omega)$, $\pm 30\%$ in both M and Γ, up to the characteristic frequency Ω of 250 meV (also roughly the maximum phonon frequency) where both $M(\omega)$ and $\Gamma(\omega)$ have begun to deviate from their low-T, low-energy Fermi liquid forms $M(\omega) = -\lambda\omega$, $\Gamma(\omega) = B(T) + C\lambda\omega^2$ for some constant C, and we use a thermal broadening $B(200\,\mathrm{K}) = 7$ meV. The slope $-\partial M(\omega)/\partial\omega|_{\omega=0} = \lambda$ gives the quasiparticle mass enhancement $m^*/m_b = 1 + \lambda \sim 3$ over the band mass m_b. The inverse scattering rate Γ peaks at a value of 0.6 eV at $|\omega| \approx 1.5\Omega$. Above 2Ω both parts of Σ become slowly varying, with $M(\omega < -2\Omega) \approx -0.2$ eV for occupied states, $\Gamma(|\omega| > 2\Omega) \approx 0.3$ eV. Note that above $|\omega| \approx 2\Omega$, M is not particle-hole symmetric.

A. Interacting band structure

The band-resolved spectral density $A_{kn}(\omega) \equiv |\mathrm{Im}G_{kn}(\omega)|/\pi$, which is the interacting counterpart of the Kohn-Sham band structure and the quantity measured in angle-resolved photoemission probes, is shown as a heat map in Fig. 1(d). This plot, with an enlargement of the low-energy region in the inset, reveals several impacts of EPC. (1) The first is the mass enhancement (flattening) of the sharp, low-energy quasiparticle bands by the factor $1 + \lambda$ at the chemical potential $\mu = 0$. (2) The coherent mass enhancement "boils away" abruptly just above $\omega \sim \Omega$, giving way at higher energies to a substantial 0.3–0.5 eV broadening around spectral density peaks that are displaced by ~ 0.2 eV from the Kohn-Sham bands. (3) The transition region reveals the "knee" or waterfall transition from coherent to incoherent that is a signature of strong EPC. This knee has received much attention in cuprate high temperature superconductor [29].

B. Spectral density

The zone-averaged electron spectral density is given by $A(\omega) = \frac{1}{\pi}\sum_{k,n}|\mathrm{Im}G_{k,n}(\omega)|$. We approximate by using a (k, n)-averaged self-energy $\Sigma(\omega)$, essentially equal to the red band data plotted in Fig. 1(c). (For small ω the self-energy presented by Kudryashov *et al.* [30] is similar since both satisfy the Fermi liquid conditions mentioned above. For larger ω there are strong differences due to approximations made in their work; see the Supplemental Material [31].)
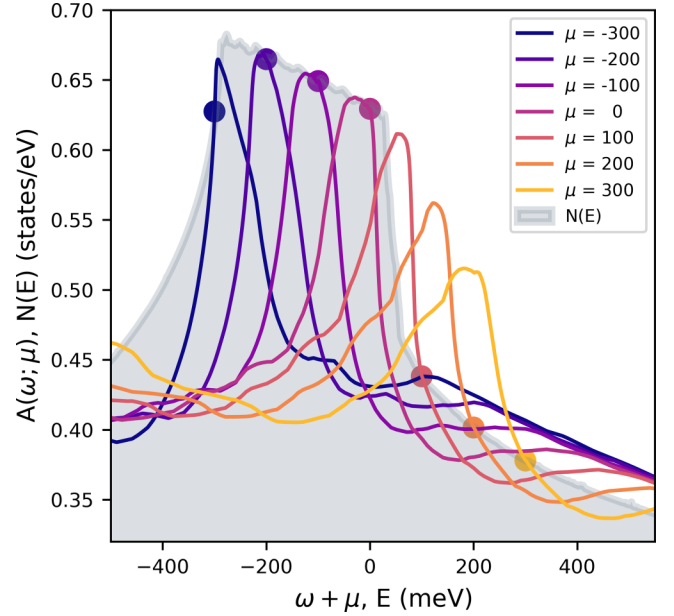

FIG. 2. Doping dependence of spectral density. Dependence of the spectral density $A(\omega)$ on chemical potential μ, calculated from Eq. (1) at 200 K. The dot on each graph marks the analytic low-temperature constraint $A(\omega = 0; \mu) = N(\mu)$, and the shaded region denotes $N(E)$. The strong particle- ($\mu > 0$) hole ($\mu < 0$) asymmetry is reflected in the simple translation of the peak for hole doping, while for particle doping the peak structure becomes highly asymmetric around μ.

The spectral function calculation simplifies to

$$A(\omega; \mu) = \int \frac{dE \ \ N(E)\,|\Gamma(\omega)|/\pi}{[\omega - (E - \mu) - M(\omega)]^2 + [\Gamma(\omega)]^2}. \quad (1)$$

This expression has the form of a Lorentzian broadening of $N(E)$, but with an energy shift $M(\omega)$ and broadening $\Gamma(\omega)$ that varies with ω. For comparison with experiment, the chemical potential $\mu = \mu(T)$ would need to be shifted to enforce conservation of the particle number. Near the chemical potential where Γ becomes very small, this expression reduces to a δ function, and the behavior is $A(\omega) \approx N([1 + \lambda]\omega)$. Thus the energy variation is enhanced by $1 + \lambda \approx 3$, which results in the *strong narrowing* of the peak in $A(\omega)$ compared to that in $N(E)$; this often unrecognized aspect is evident in Fig. 1(b).

When $N(E)$ is constant over an energy range of a several Ω as in most metals and as assumed in textbooks, redistribution of spectral density is transparent to most probes. With sharp, asymmetric structure in $N(E)$ on the scale of Ω the effect is dramatic. Due to the Fermi liquid requirements listed above, Eq. (1) gives $A(\omega = 0; \mu) = N(E = \mu)$, which is reproduced in the calculation, as shown in Figs. 1(c) and 2.

We compare in Fig. 2, referenced to the underlying electronic DOS, the spectral density calculated for several band fillings at chemical potential μ, neglecting changes in $\Sigma(\omega)$. The very strong asymmetry around the physical band filling of H_3S is evident. For zero or negative values of μ, the spectral density remains a strongly compressed version of $N(E)$ and is displaced downward rigidly with μ across the plateau of
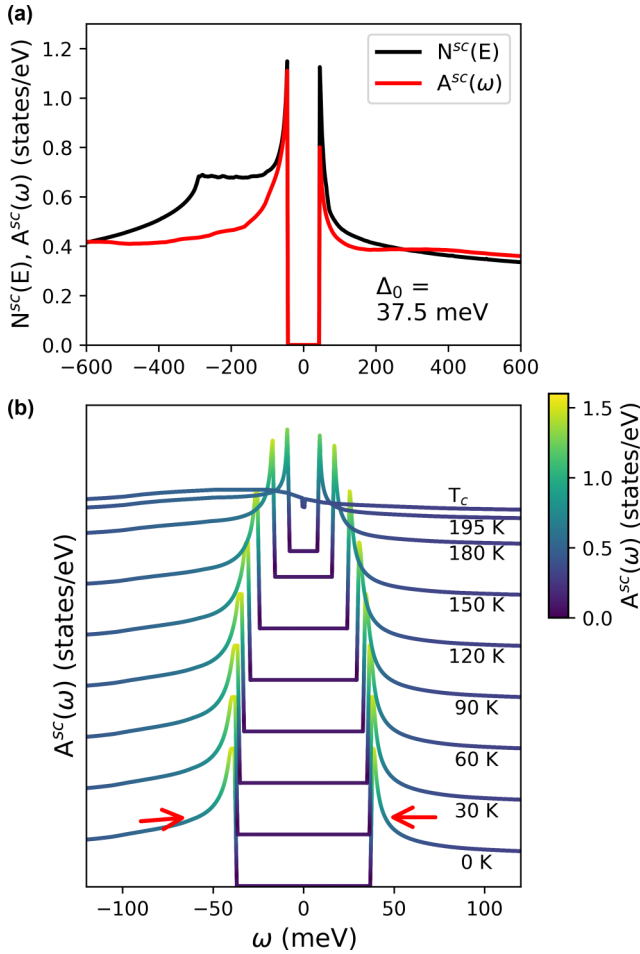
FIG. 3. Spectral density of H_3S in the superconducting state. (a) Comparison at $T = 0$ without (black) and with (red) the self-energy included. The strong particle-hole asymmetry across the gap is evident. The gap $2\Delta = 75$ meV is the measured value [32]. (b) Temperature evolution of the spectral density $A^{sc}(\omega)$ through the $T = 0$–200 K range, with constant vertical shifts of the curves. The color bar denotes the spectral intensity, and the red arrows point to 0.8 eV^{-1} on either side of the gap, highlighting the particle-hole asymmetry.

$N(E)$. For electron doping, however, as μ passes across the upper vHs onto the steep slope, $A(\omega; \mu)$ peaks not at $\omega = 0$ but at negative ω. Doping (μ) in effect drags the spectral density peak along with it for up to and beyond Ω above the intrinsic chemical potential. This asymmetry will induce behaviors of thermodynamic, transport, and low-energy spectra that are quite different from what would be obtained from the bare spectrum, with the differences arising from the strong p-h *asymmetry*.

C. Effect of the superconducting gap

Careful treatment of T dependences would require real-frequency-axis solutions of generalized Eliashberg equations (treating $N(E)$ [17]), which are not available. Instead, standard BCS expressions can be adopted to allow demonstration of the implications of the vHs on the electronic spectral density. In Fig. 3 we show the impact on $N(E)$ of opening

a superconducting BCS gap,

$$A^{sc}(\omega) = \int d\omega' A(\omega') \frac{\omega'}{\sqrt{(\omega' - \omega)^2 - \Delta^2}}, \quad (2)$$

with an analogous gap-opening expression for $N^{sc}(E)$ (with $\omega' \to E$). The temperature dependence of the gap follows the approximate analytic form $2\Delta(T) = 2\Delta_o[1 - (T/T_c)^2]^{1/2}$, with $2\Delta_o \approx 5k_BT_c = 75$ meV. Figure 3(a) illustrates the great difference between $N_{sc}(E)$ and $A_{sc}(\omega)$, each displaying the strong particle-hole asymmetry imparted by the vHs.

Figure 3(b) displays the dependence on temperature of the quasiparticle spectrum $A_{sc}(\omega)$. The temperature dependence of $\Sigma(\omega)$ can be neglected since T_c, although at a record high value, is still low compared to phonon frequencies. The gap remains sharp, and the spectrum remains asymmetric until it assumes its normal-state form at T_c.

IV. THERMAL DISTRIBUTION FUNCTION

When $\Sigma_{kn}(\omega)$ depends on k, n only through E_{kn}, as is reasonably assumed for H_3S [with the same holding for $A_{kn}(\omega)$], it is simple to show [33,34] that for certain thermodynamic properties, the effect of interactions can be transferred to the thermal distribution function $f(\omega)$, the interacting counterpart of the noninteracting Fermi-Dirac distribution $f_o(E)$. In Matsubara space, the definition in terms of the Green's function leads to ($k_B = 1 = \hbar$ units, $\mu = 0$)

$$f(E_{kn}, T; \mu) \equiv T \sum_{n=-\infty}^{+\infty} G(kn, i\omega_n; \mu)e^{i\omega_n\eta}$$

$$= \int d\omega f_0(\omega)|\frac{1}{\pi}\text{Im}G(kn, \omega; \mu)|$$

$$\to \int d\omega \frac{f_0(\omega)|\Gamma(\omega)|/\pi}{[\omega - E_{kn} - M(\omega)]^2 + [\Gamma(\omega)]^2}, \quad (3)$$

upon continuing back to the real-frequency axis and then using the k-averaged, hence k-independent, self-energy. In this equation $\omega_n = (2n + 1)\pi T$ is the Matsubara frequency, and η is a positive infinitesimal.

Along with the calculated spectral density, this allows one to write the electron number in three different ways, beginning with the noninteracting Kohn-Sham electron number $\mathcal{N}$ from the first expression $(E_F = 0)$:

$$\mathcal{N} = \int dE f_0(E; T = 0)N(E)$$

$$= \int d\omega f_0(\omega - \mu; T)A(\omega; \mu) \quad (4)$$

$$= \int dE f(E - \mu, T; \mu)N(E). \quad (5)$$

The second relation determines $\mu(T)$, an estimation of which is provided in the Supplemental Material. The second and third expressions together express that, for the (conserved) particle number, the effect of interactions on $\mathcal{N}$ can be shifted between an interacting density of states $A(\omega; \mu)$ and an interacting thermal distribution function $f(E - \mu, T; \mu)$. Equation (5) is a simple example of a general result obtained by Lee and Yang [35] that thermodynamic quantities can be obtained
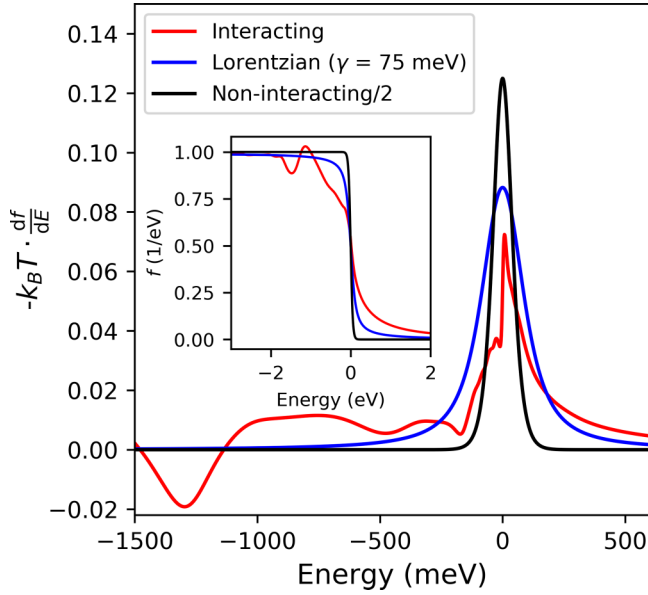
FIG. 4. Interacting thermal distribution calculated at 300 K. The dimensionless derivative of the thermal occupation $-k_B T \frac{\partial f(E-\mu, T; \mu)}{\partial E}$ (red line), contrasted with that of the noninteracting Fermi-Dirac distribution, divided by 2 to fit on the same scale (black line). Also shown, to emphasize the difference in shape (blue line), is an interacting thermal distribution calculated using a fictitious spectral density of a Lorentzian form with a half width at half maximum of 75 meV. Interaction not only results in the expected broadened of $f(E; \mu)$, but also strong asymmetry in particle-hole thermal occupation emerges. The inset shows the broadening of the distribution function itself.

from thermal averages incorporating the interacting (versus noninteracting) occupation number, but in momentum space [i.e., $f(\vec{k})$ versus $f_o(\varepsilon_{\vec{k}})$].

This interacting thermal distribution function reflects how noninteracting states $[N(E)]$ are sampled by the interacting system, rather than the conventional formulation in which interacting kernels are sampled over the noninteracting thermal distribution. Figure 4 provides the derivative $-T \frac{\partial f(E, T; \mu)}{\partial E}$. The interacting distribution differs strongly in the region of strong variation of $N(E)$. Unlike the symmetric derivative of the Fermi-Dirac distribution, the interacting version becomes asymmetric according to the behavior of $\Sigma(E)$ convoluted with the structure imposed by the vHs. Contrary to intuition, with interactions the thermal occupation is not limited to the interval [0,1], although excursions outside this range will have a limited effect.

The primary effect, shown in Fig. 4, is significant redistribution leading to a strong distortion from particle-hole symmetry. To illustrate the point that the spectral function has a form qualitatively different from Lorentzian broadening, we also show in Fig. 4 a convolution of the noninteracting Fermi-Dirac distribution with a Lorentzian of half width $\gamma = 75$ meV. This model (and p-h-symmetric) distribution lacks the qualitative features of the real interacting distribution.

V. INFRARED SPECTRUM

Infrared spectroscopy is an important probe of the effects of EPC in superconductors. While a general study of the
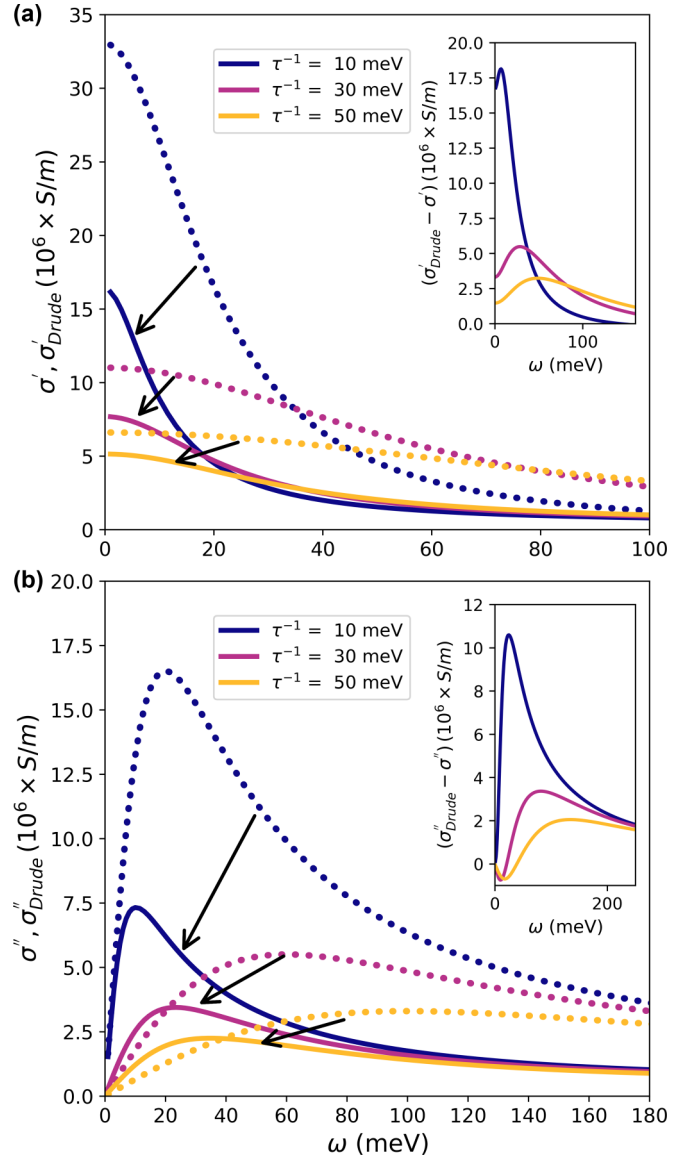

FIG. 5. Infrared optical conductivity of H$_3$S. (a) Real and (b) imaginary parts of the conductivity in the normal-state H$_3$S, comparing the generalized Drude expression of Eq. (7) (solid lines) with the noninteracting $[\Sigma(\omega) = 0]$ limit (dotted lines), at $T = 200$ K. Results are shown for three values of the elastic scattering rate $1/\tau$. The insets show the differences as indicated.

effect of vHs awaits further developments, something can be said about the far infrared, where interband transitions are negligible. Capitani *et al.* [32] have reported the observed and modeled reflectivity in H$_3$S at high pressure, observing a structure identified with an energy scale of 160 meV, suggested to be a phonon with a very strong infrared coupling that is not evident from current theory. Given the paucity of experiments that are possible at high pressure, this experiment assumes an unusually strong impact.

Without EPC, the intraband optical conductivity reduces to the Drude form $\sigma(\omega) = \sigma_o/(1 - i\omega\tau)$, where

$$\sigma_o = e^2 N(0) \frac{v_F^2}{3} \tau = e^2 \left(\frac{n}{m} \right)_{\text{eff}} \tau \equiv \frac{\omega_p^2 \tau}{4\pi} \tag{6}$$

gives the zero-frequency limit in terms of $N(0)$ and the mean Fermi surface velocity [5] $v_F = 2.5 \times 10^7$ cm/s, which combines with $N(0)$ to give the Drude plasma frequency $\omega_p = 2.8$ eV for H_3S. In the general expression for the current-current correlation function that gives $\sigma(\omega)$, the vertex matrix elements are simply the electron velocity v_k. In the average over the Fermi surface, the velocity factors cancel the contributions from the vHs regions, making the ubiquitous "constant-DOS" treatment reasonable. Allen has given the corresponding generalized Drude (intraband) expression [36] for an interacting system,

$$\sigma(\omega) = i \frac{\omega_p^2}{4\pi} \int d\omega' \frac{[f(\omega') - f(\omega' + \omega)]/\omega}{\omega - \Sigma(\omega' + \omega) + \Sigma^*(\omega')}. \quad (7)$$

The integral gives an effective $\tau_{\text{eff}}(\omega)$. Results with additional elastic scattering values of $1/\tau = 10, 30, 50$ meV are displayed in Fig. 5. Inelastic scattering due to EPC causes a reduction (shown by the arrows) in the real component of the conductivity as it approaches its static dc value at small ω. The $(1 + \lambda)$ mass enhancement shows up in the imaginary part, where it translates to an increased slope in the low-frequency linear regime as well as a strong reduction in the magnitude. These results do not resolve the origin of the feature studied by Capitani *et al.* [32]. The calculated reflectivity at four values of τ is provided in the Supplemental Material [31].

VI. SUMMARY

In this work we have demonstrated the strong impact of large electron-phonon coupling on the fermionic spectral density and band renormalization of the high-temperature superconductor H_3S, which causes qualitatively new and anti-intuitive phenomena due to its interplay with the sharp and asymmetric DOS peak at the Fermi level, caused by two neighboring (in energy) Van Hove singularities. The picture of a simple smeared spectral density is conceptually incorrect and quite misleading; at low temperature, of the order of T_c or even a little higher, the peak becomes *sharper* (narrower) than the density of states peak due to the coherence that also gives the mass enhancement effect. Peculiarly, the sharp spectral density peak follows the chemical potential with doping, but in a strongly particle-hole asymmetric way. In the superconducting regime as well, strong particle-hole asymmetry occurs as a consequence of the Van Hove singularities. We further elucidate the effect of electron-phonon coupling on the infrared conductivity for consideration in interpretation of optical data.

[1] A. P. Drozdov, M. I. Eremets, I. A. Troyan, V. Ksenofontov, and S. I. Shylin, Conventional superconductivity at 203 kelvin at high pressures in the sulfur hydride system, Nature (London) **525**, 73 (2015).

[2] M. Einaga, M. Sakata, T. Ishikawa, K. Shimizu, M. I. Eremets, A. P. Drozdov, I. A. Troyan, N. Hirao, and Y. Ohishi, Crystal structure of the superconducting phase of sulfur hydride, Nat. Phys. **12**, 835 (2016).

[3] D. Duan, Y. Liu, Y. Ma, Z. Shao, B. Liu, and T. Cui, Structure and superconductivity of hydrides at high pressure, Natl. Sci. Rev. (China) **4**, 121 (2017).

[4] D. Duan, Y. Liu, F. Tian, D. Li, X. Huang, Z. Zhao, H. Yu, B. Liu, W. Tian, and T. Cui, Pressure-induced metalization of dense $(H_2S)_2H_2$ with high-T_c superconductivity, Sci. Rep. **4**, 6968 (2014).

[5] N. Bernstein, C. S. Hellberg, M. D. Johannes, I. I. Mazin, and M. J. Mehl, What superconducts in sulfur hydrides under pressure and why, Phys. Rev. B **91**, 060511(R) (2015).

[6] D. A. Papaconstantopoulos, B. M. Klein, M. J. Mehl, and W. E. Pickett, Cubic H_3S around 200 GPa: An atomic hydrogen superconductor stabilized by sulfur, Phys. Rev. B **91**, 184511 (2015).

[7] J. A. Flores-Livas, A. Sanna, and E. K. U. Gross, High temperature superconductivity in sulfur and selenium hydrides at high pressure, Eur. Phys. J. B **89**, 63 (2016).

[8] C. Heil and L. Boeri, Influence of bonding on superconductivity in high-pressure hydrides, Phys. Rev. B **92**, 060508(R) (2015).

[9] R. Akashi, M. Kawamura, S. Tsuneyuki, Y. Nomura, and R. Arita, First-principles study of the pressure and crystal-structure dependences of the superconducting transition temperature in compressed sulfur hydrides, Phys. Rev. B **91**, 224513 (2015).

[10] I. Errea, M. Calandra, C. J. Pickard, J. Nelson, R. J. Needs, Y. Li, H. Liu, Y. Zhang, Y. Ma, and F. Mauri, High-Pressure Hydrogen Sulfide from First Principles: A Strongly Anharmonic Phonon-Mediated Superconductor, Phys. Rev. Lett. **114**, 157004 (2015).

[11] Y. Ge, F. Zhang, and Y. Yao, First-principles demonstration of superconductivity at 280 K in hydrogen sulfide with low phosphorus substitution, Phys. Rev. B **93**, 224513 (2016).

[12] W. Sano, T. Koretsune, T. Tadano, R. Akashi, and R. Arita, Effect of Van Hove singularities on high-T_c superconductivity in H_3S, Phys. Rev. B **93**, 094525 (2016).

[13] L. Liu, C. Wang, S. Yi, K, W. Kim, J. Kim, and J.-H. Cho, Microscopic mechanism of room-temperature superconductivity in compressed LaH_{10}, Phys. Rev. B **99**, 140501(R) (2019).

[14] Y. Quan and W. E. Pickett, Van Hove singularities and spectral smearing in high-temperature superconducting H_3S, Phys. Rev. B **93**, 104526 (2016).

[15] I. Errea, M. Calandra, C. J. Pickard, J. R. Nelson, R. J. Needs, Y. Li, H. Liu, Y. Zhang, Y. Ma, and F. Mauri, Quantum hydrogen-bond symmetrization in the superconducting hydrogen sulfide system, Nature (London) **532**, 81 (2016).

[16] J. Labbé, S. Barišić, and J. Friedel, Strong-Coupling Superconductivity in V_3X Type of Compounds, Phys. Rev. Lett. **19**, 1039 (1967).

[17] W. E. Pickett, Generalization of the theory of the electron-phonon interaction: Thermodynamic formulation of superconducting- and normal-state properties, Phys. Rev. B **26**, 1186 (1982).

[18] S. Engelsberg and J. R. Schrieffer, Coupled electron-phonon system, Phys. Rev. **131**, 993 (1963).

[19] K. Shimojima and H. Ichimura, Spectral weight function and electron momentum distribution in the normal electron-phonon system, Prog. Theor. Phys. **43**, 925 (1970).

[20] P. Giannozzi, S. Baroni, N. Bonini, M. Calandra, R. Car, C. Cavazzoni, D. Ceresoli, G. L. Chiarotti, M. Cococcioni, I. Dabo *et al.*, QUANTUM ESPRESSO: A modular and open-source software project for quantum simulations of materials, J. Phys. Condens. Matter **21**, 395502 (2009).

[21] P. Giannozzi, O. Andreussi, T. Brumme, O. Bunau, M. Buongiorno Nardelli, M. Calandra, R. Car, C. Cavazzoni, D. Ceresoli, M. Cococcioni *et al.*, Advanced capabilities for materials modeling with QUANTUM ESPRESSO, J. Phys. Condens. Matter **29**, 465901 (2017).

[22] J. P. Perdew, K. Burke, and M. Ernzerhof, Generalized Gradient Approximation Made Simple, Phys. Rev. Lett. **77**, 3865 (1996).

[23] D. J. Scalapino, J. R. Schrieffer, and J. W. Wilkins, Strong-coupling superconductivity. I, Phys. Rev. **148**, 263 (1966).

[24] F. Giustino, Electron-phonon interactions from first principles, Rev. Mod. Phys. **89**, 015003 (2017).

[25] A. A. Mostofi, J. R. Yates, Y.-S. Lee, I. Souza, D. Vanderbilt, and N. Marzari, wannier90: A tool for obtaining maximally-localised Wannier functions, Comput. Phys. Commun. **178**, 685 (2008).

[26] F. Giustino, M. L. Cohen, and S. G. Louie, Electron-phonon interaction using Wannier functions, Phys. Rev. B **76**, 165108 (2007).

[27] S. Poncé, E. R. Margine, C. Verdi, and F. Giustino, EPW: Electron-phonon coupling, transport and superconducting properties using maximally localized Wannier functions, Comput. Phys. Commun. **209**, 116 (2016).

[28] E. R. Margine and F. Giustino, Anisotropic Migdal-Eliashberg theory using Wannier functions, Phys. Rev. B **87**, 024505 (2013).

[29] T. Cuk, F. Baumberger, D. H. Lu, N. Ingle, X. J. Zhou, H. Eisaki, N. Kaneko, Z. Hussain, T. P. Devereaux, N. Nagaosa, and Z.-X. Shen, Coupling of the B_{1g} Phonon to the Antinodal Electronic States of $Bi_2Sr_2Ca_{0.92}Y_{0.08}Cu_2O_{8+\delta}$, Phys. Rev. Lett. **93**, 117003 (2004).

[30] N. A. Kudryashov, A. A. Kutukov, and E. A. Mazur, Normal state of metallic hydrogen sulfide, Phys. Metals Metallogr. **118**, 113 (2017).

[31] See Supplemental Material at http://link.aps.org/supplemental/10.1103/PhysRevB.100.094521 where additional explanation of the self-energy and spectral density is given. Plots of the absolute infrared optical reflectivity are also provided.

[32] F. Capitani, B. Langerome, J.-B. Brubach, P. Roy, A. Drozdov, M. I. Eremets, E. J. Nicol, J. P. Carbotte, and T. Timusk, Spectroscopic evidence of a new energy scale for superconductivity in H_3S, Nat. Phys. **13**, 859 (2017).

[33] W. E. Pickett, Renormalized Thermal Distribution Function in an Interacting Electron-Phonon System, Phys. Rev. Lett. **48**, 1548 (1982).

[34] B. Mitrović and J. Carbotte, Superconducting T_c for the separable model of $(\varepsilon, \varepsilon')$ variation in $\alpha^2F(\varepsilon, \varepsilon'; \Omega)$, Phys. Rev. B **28**, 2477 (1983).

[35] T. D. Lee and C. N. Yang, Many-body problem in quantum statistical mechanics. IV. Formulation in terms of average occupation number in momentum space, Phys. Rev. **117**, 22 (1960).

[36] P. B. Allen, Electron self-energy and generalized Drude formula for infrared conductivity of metals, Phys. Rev. B **92**, 054305 (2015).